Journal of
Biomedical Optics

SPIEDigitalLibrary.org/jbo

Flux density calibration in diffuse optical tomographic systems

Samir Kumar Biswas
Kanhirodan Rajan
Ram M. Vasu

Journal of Biomedical Optics 18(2), 026023 (February 2013)

Flux density calibration in diffuse optical tomographic systems

Samir Kumar Biswas,[a] Kanhirodan Rajan,[a] and Ram M. Vasu[b]
[a]Indian Institute of Science, Department of Physics, Bangalore, India
[b]Indian Institute of Science, Department of Instrumentation and Applied Physics, Bangalore, India

Abstract. The solution of the forward equation that models the transport of light through a highly scattering tissue material in diffuse optical tomography (DOT) using the finite element method gives flux density (Φ) at the nodal points of the mesh. The experimentally measured flux (U_{measured}) on the boundary over a finite surface area in a DOT system has to be corrected to account for the system transfer functions (R) of various building blocks of the measurement system. We present two methods to compensate for the perturbations caused by R and estimate true flux density (Φ) from $U_{\text{measured}}^{\text{cal}}$. In the first approach, the measurement data with a homogeneous phantom ($U_{\text{measured}}^{\text{homo}}$) is used to calibrate the measurement system. The second scheme estimates the homogeneous phantom measurement using only the measurement from a heterogeneous phantom, thereby eliminating the necessity of a homogeneous phantom. This is done by statistically averaging the data ($U_{\text{measured}}^{\text{hetero}}$) and redistributing it to the corresponding detector positions. The experiments carried out on tissue mimicking phantom with single and multiple inhomogeneities, human hand, and a pork tissue phantom demonstrate the robustness of the approach. [DOI: 10.1117/1.JBO.18.2.026023]

Keywords: flux density estimation; optical tomography; instrumentation.

Paper 12751R received Nov. 21, 2012; revised manuscript received Jan. 15, 2013; accepted for publication Jan. 31, 2013; published online Feb. 19, 2013.

1 Introduction

Diffuse optical tomography (DOT)[1–6] is one of the emerging noninvasive functional imaging modalities.[1,3] To study the regional physiological process in highly scattering media such as tissue, a low-energy, near infrared (NIR) light-based imaging technique is one of the best in terms of quantitative recovery of spectroscopic optical parameters. The main goal is to recover the spatial variation of optical properties, which can be used to diagnose the different metabolic states of tissue. An iterative reconstruction algorithm[1–3] attempts to recover the optical properties such as absorption (μ_a) and reduced scattering coefficients (μ_s') by repeatedly solving the forward problem and updating μ_a and μ_s' based on the difference between measurement data and the forward prediction. System calibration is an important issue in a variety of applications such as DOT imaging,[7–14] fluorescence imaging,[15] electrical impedance tomography,[16] photoacoustic tomography,[17] ultrasound assisted optical imaging, thermal imaging, and defect detection in civil engineering. The reconstruction depends on experimental measurements, and the iteration is continued until the experimental measurement matches the forward prediction. In DOT, the data calibration is often performed using a homogeneous reference phantom.[8–14] Tarvainen et al.[9] have discussed a calibration strategy with homogeneous data. One way to compensate for the measurement error is to use difference imaging, which is known to produce images with few artifacts.[8,9] However, this method cannot be used when absolute optical properties are required or when a reference measurement is not available. We need to devise ways to obviate the need for a "background" homogeneous data set for the difference imaging approach. That said, the focus of this study is to estimate a background image for difference imaging without taking a separate background measurement. The calibrated absolute flux density by adequately modeling the measurement process by either analytic or numerical methods is a must for good reconstructed images.[8–14] In DOT imaging, total flux (U_{measured}) measured by a detector over a finite area has to be calibrated to account for the system response function (R) before it is plugged into the optimization algorithm. The estimation of response functions that comprises the quantum conversion efficiency (Q) of the photo multiplier tube (PMT), coupling factor (C), laser source strength (S), fiber loss (L), free propagation of light (Γ),[4] and transfer function (H) of the measurement system is quite tedious. Calibrating the measurement data to account for all these aberrations is an iterative method[4,13] where estimating flux density (J_n) (see Ref. 4) requires the inversion of Eq. (2) with the prior information of all instrumental response functions.[8,13] The calibration process requires experimental homogeneous data (measurement data with a homogeneous phantom),[8,9,12,13] instrument calibration, and various offset terms.[8,9,11,13]

In this context, we modified Eq. (3) of Ref. 4 by incorporating various instrumental response functions (R) and arrived at a simple absolute flux density estimation scheme [Eqs. (1)–(6)] (Scheme 1) that uses homogeneous measurement data ($U_{\text{measured}}^{\text{homo}}$) and a background optical parameter, which is measured by a standard method.[18] We reconstructed the absolute optical property of pork tissue phantom, human tissue, and tissue-mimicking phantoms.

However, in practical situations such as in a clinical application, the homogeneous measurement data will not be available. For such situations, a scheme (Scheme 2) is proposed to estimate

---

Address all correspondence to: Kanhirodan Rajan, Indian Institute of Science, Department of Physics, Bangalore, India. Tel: +91-80-22933280; Fax: +91-80-23602602; E-mail: rajan@physics.iisc.ernet.in

a homogeneous data from a heterogeneous phantom measurement. In such a scheme, the homogeneous data are estimated ($U^{\text{est-homo}}_{\text{measured}}$) by statistically averaging the heterogeneous measurement data ($U^{\text{hetero}}_{\text{measured}}$) and redistributing them to the corresponding detector positions [Eq. (7)]. The estimated homogeneous ($U^{\text{est-homo}}_{\text{measured}}$) data is used[13,19] to estimate the initial background optical parameters and the flux density [Eq. (8)]. Using this approach, we reconstructed absolute optical property distribution of tissue-mimicking phantoms, pork tissue, and human tissue.

2 Calibration of Measurement Data

2.1 *Calibration of Heterogeneous Measurement Data Using Homogeneous Data*

The transport of light through a diffusive medium such as tissue is modeled through the diffusion equation,[2,3] given as $[-\nabla\cdot\kappa(r)\nabla+\mu_a(r)]\Phi(r)=S(r)$, where $\kappa(r)=1/3[\mu_a(r)+\mu_s'(r)]$. The forward model is solved[2] over the domain (V) to estimate the flux density ($\Phi^{\text{predicted}}=\mathcal{M}[\Phi]$) on the surface boundary (Ω). $\mathcal{M}:\ L_2(V)\rightarrow L_2(\Omega)$ is the measurement operator. Due to the spatial ($r\in V,\ \Omega$) variation of the optical parameter $[\Delta\mu^i(r)]$, the perturbation equation in terms of the optical parameter can be written in a Taylor series expansion, retaining only the first derivative, as[20]

$$\Delta M^i=\Phi^{\text{cal}}_{\text{measured}}-\Phi^{\text{predicted}(i)}=F'(\mu^i)[\Delta\mu^i] \\ \mu^{i+1}(r)=\mu^i(r)+\Delta\mu^i(r), \tag{1}$$

where (F') is the Jacobian matrix [1, 3, 20] of forward operator F, ΔM^i is the difference between the calibrated experimental flux density ($\Phi^{\text{cal}}_{\text{measured}}$) and the forward model predicted flux density ($\Phi^{\text{predicted}(i)}$) at the i'th iteration. Now, we will present a few mathematical equations by which flux density will be estimated from total detected flux, U_{measured}.

The free space light propagation [Fig. 1(a)] from phantom surface to detector[4] is given as

$$\Gamma(r,r_d)=\xi(r,r_d)\times\frac{f(\text{NA}-\sin\theta_d)}{|r_d-r|^2}\cos\theta\cos\theta_d dA,$$

where $r=|\vec{r'}-\vec{r^k}|$, $[r_k,r'\in V,\Omega]$, $\xi(r,r_d)$ is the visibility factor, $\cos\theta=\hat{\zeta}.\hat{n}$ is the cosine dependent on Lambert's law, $\hat{\zeta}$ is the power radiation direction on surface Ω, NA is the numerical aperture of fiber, θ_d is the detector orientation with respect to the line of sight, and r_d is the distance between detector and surface (Ω) (see Ref. 4). With an inhomogeneity of dia $=2r^{\text{incl}}$ with (μ_a^{incl}, $\mu_s'^{\text{incl}}$) embedded in the homogeneous phantom, the total flux over the fiber cross-section (dA) measured by the lock-in amplifier can be written as

$$^{k,d}U^{\text{hetero}}_{\text{measured}}=\frac{Q^{k,d}\cdot H^{k,d}\cdot L^{k,d}}{\pi} \\ \times\int_\Omega C^{k,d}(r,r_d)J_n^{k,d}(S_k,r)\Gamma^{k,d}(r,r_d)\mathrm{d}\Omega, \tag{2}$$

where $(\mu_a,\mu_s')=(\mu_a^0,\mu_s'^0)\cup(\mu_a^{\text{incl}},\mu_s'^{\text{incl}})$ and $J_n^{k,d}(S_k,r)$, is the outgoing normal flux density at the surface ($d\Omega$) of the phantom for a particular source position k (S_k, $k=1\ldots N=12$) and detector position d (D_d, $d=-m\ldots m$). For a medium with a homogeneous distribution of μ_a^0, $\mu_s'^0$ over the domain, the outgoing normal flux density at the surface is $J_{n,0}^{k,d}(S_k,r)$ and the total flux measured by the lock-in amplifier can be written as

$$^{k,d}U^{\text{homo}}_{\text{measured}}=\frac{Q^{k,d}\cdot H^{k,d}\cdot L^{k,d}}{\pi} \\ \times\int_\Omega C^{k,d}(r,r_d)J_{n,0}^{k,d}(S_k,r)\Gamma^{k,d}(r,r_d)\mathrm{d}\Omega. \tag{3}$$

Scaling the experimentally measured heterogeneous data ($^{k,d}U^{\text{hetero}}_{\text{measured}}$) by $\Phi^{\text{predicted}(0)}/^{k,d}U^{\text{homo}}_{\text{measured}}$ where ($^{k,d}U^{\text{homo}}_{\text{measured}}$) is the experimentally measured homogeneous data for source k and detector d position, the calibrated experimental heterogeneous flux ($\Phi^{\text{cal hetero}}_{\text{measured}}$) can be written for the k'th source and the d'th detector as

$$^{k,d}\Phi^{\text{cal hetero}}_{\text{measured}}=\frac{^{k,d}U^{\text{hetero}}_{\text{measured}}}{^{k,d}U^{\text{homo}}_{\text{measured}}}\times{}^{k,d}\Phi^{\text{predicted}(0)}(r) \\ =\frac{\frac{Q^{k,d}\cdot H^{k,d}\cdot L^{k,d}}{\pi}\int_\Omega C^{k,d}S_kJ_n^{k,d}(r)\Gamma^{k,d}\mathrm{d}\Omega}{\frac{Q^{k,d}\cdot H^{k,d}\cdot L^{k,d}}{\pi}\int_\Omega C^{k,d}S_kJ_{n,0}^{k,d}(r)\Gamma^{k,d}\mathrm{d}\Omega} \\ \times\Phi^{\text{predicted}(0)}(r), \tag{4}$$

where we used the property $J_n\propto S_k$ (when other parameters are fixed) [Fig. 1(b) and 1(c)]. With known background optical parameters $(\mu_a^0,\mu_s'^0)$, the simulated homogeneous flux density (at iteration $i=0$) at the surface can be written as $\Phi^{\text{predicted}(0)}(r)=J_{n,0}^{k,d}$. We make an assumption that when ($dA\ll\Omega$), the system transfer function does not vary over

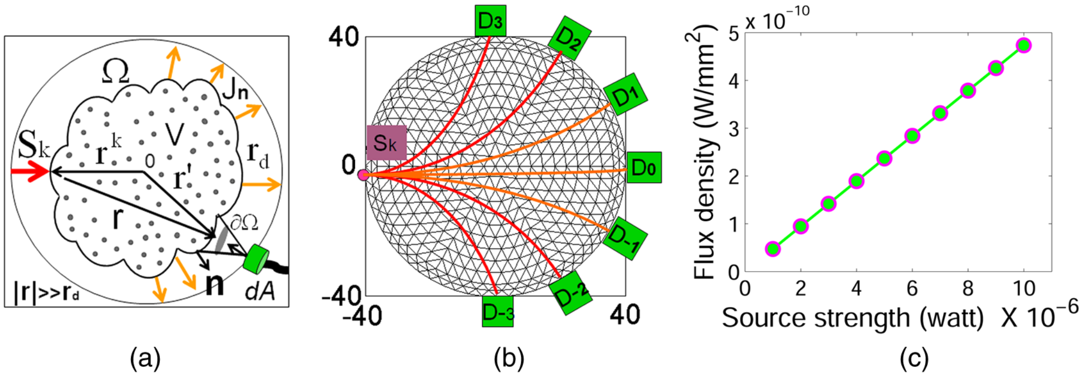

Fig. 1 (a) Experimental model; (b) simulated domain and data collection model; (c) source strength versus flux density at detector $D_{d=3}$. The source intensity is given over a single boundary element, and detection has taken place at the boundary node.

the cross-section of the fiber bundle (either with or without inhomogeneity) and the calibrated flux density then can be written as

$$ {}^{k,d}\Phi^{\mathrm{cal}}_{\mathrm{measured}} = \frac{\frac{Q^{k,d}\cdot H^{k,d}\cdot L^{k,d}}{\pi}}{\frac{Q^{k,d}\cdot H^{k,d}\cdot L^{k,d}}{\pi}} \times \frac{C^{k,d} S_k \Gamma^{k,d} \Omega J_n^{k,d}(r)}{C^{k,d} S_k \Gamma^{k,d} \Omega J_0^{k,d}(r)} \times J_{n,0}^{k,d}(r). \tag{5} $$

The calibrated experimental heterogeneous flux density for the k'th source and the d'th detector is reduced to

$$ {}^{k,d}\Phi^{\mathrm{cal\,hetero}}_{\mathrm{measured}} = J_n^{k,d}. \tag{6} $$

2.2 *Estimation of Homogeneous Data from a Heterogeneous Phantom Measurement*

Breast tissue is considered conical, with cross-sections approximated by circles. We show that the calibrated heterogeneous flux density at the surface of the phantom (dia $= 2R'$) can be deduced even when prior experimental homogeneous data is not available. The homogeneous data can be estimated (${}^{k,d}U^{\mathrm{est-homo}}_{\mathrm{measured}}$) from experimental heterogeneous data (${}^{k,d}U^{\mathrm{hetero}}_{\mathrm{measured}}$) by statistically averaging the heterogeneous data for all source locations $k(\forall\ k)$ to a particular detector position ($d = m$) and redistributing them to the corresponding detector positions. The detector D_0 is at the diametrically opposite side of source S_k [Fig. 1(b)]. There are detectors D_2, D_4, D_6 and D_{-2}, D_{-4}, D_{-6} in equally spaced positions on either side of D_0 for gathering output data. The diffuse photons that reach the detector depend on the distance between the source and detector, the absorption and scattering coefficients of the background, and those of the inhomogeneities. For a homogeneous circular phantom, the flux density at particular detector location [e.g., at $d = D_3$ in Fig. 1(b)] will be same for a similar source-detector path (e.g., at $d = -D_3$) due to geometrical symmetry. There are seven detectors (placed at $d = -3$ to 3) for each source placement. Due to circular symmetry, the first set of detector data (for $k = 1$, $d = -3$ to 3) repeats for all source locations. This scheme is extended for estimating the homogeneous data by statistically averaging heterogeneous measurement (which compensates for the absorbed photon). The estimated homogeneous data can be written as

$$ {}^{k,d}U^{\mathrm{est-homo}}_{\mathrm{measured}} = \frac{1}{(N-f)} \sum_{\forall k} \frac{Q^{k,d}\cdot H^{k,d}\cdot L^{k,d}}{\pi} \times \int_{\Omega} C^{k,d} S_k J_{n,0}^{k,d}(r) \Gamma^{k,d} \mathrm{d}\Omega, \tag{7} $$

where f is the photon compensation factor, which has a value between 0 to $(N-1)$ and increases with effective perturbation (EP) due to inhomogeneity. The EP is defined as $\mathrm{EP} = \sum_i \pi r_i^{\mathrm{incl}2} \cdot [(\mu_{a,i}^{\mathrm{incl}}, \mu_{s,i}'^{\mathrm{incl}})]/[\pi R'^2 \cdot (\mu_a^0, \mu_s'^0)]$. By trial and error, we have found that f varies linearly with EP. The value of f is estimated by summing over the diffuse light that reaches the detector. For each source location, we make d detector measurements, and we can safely assume that at least one of these d measurements is unaffected[19] by inhomogeneity [see Fig. 1(a)]. With less inhomogeneity, the probability of such a measurement increases. This unaffected data (equivalent to a homogeneous phantom) is the maximum [$I_{n,0} = \max({}^{\forall k,d}U^{\mathrm{hetero}}_{\mathrm{measured}})$] value among all source locations for a particular detector position (say, $d = m$). Based on the Beer-Lambert absorption law, the intensity variation can be written as $I_n = I_{n,0} \exp[-r^{\mathrm{incl}}(\mu_a^{\mathrm{incl}} + \mu_s'^{0})]$. The line perturbation is $r^{\mathrm{incl}}(\mu_a^{\mathrm{incl}} + \mu_s'^{0})$. Accuracy improves as the number of source locations increases. With compensation factor f defined as $f = \sum_{k,d=m}^{12} \log(I_{n,0}/{}^{k,d}U^{\mathrm{hetero}}_{\mathrm{measured}})$, the calibrated heterogeneous flux density data can be obtained in a similar way using Eqs. (4) and (7) and is given by

$$ {}^{k,d}\Phi^{\mathrm{cal\,hetero}}_{\mathrm{measured}} = J_n^{k,d}(r). \tag{8} $$

Table 1 f_c Factor estimation using the trial and error strategy.

Trial and error method				
Inclusions	1	2	3	0
EP (%)	3.15	6.30	9.46	0
f_c	1.18	2.27	3.28	0
Error ($\bar{e}$)	0.0018	0.0022	0.0017	1.4E – 5

Table 2 f_c Factor estimation using the EP strategy.

EP method				
Inclusions	1	2	3	0
EP (%)	3.15	6.30	9.46	0
f_c	1.21	2.43	3.10	0
Error ($\bar{e}$)	0.0035	0.0150	0.0210	4.70E – 4

We also have estimated the value of f based on EP by the trial-and-error approach for a phantom with a single inhomogeneity, as well as multiple embedded inhomogeneities. Tables 1 and 2 present the corresponding f values and the errors for various inhomogeneities.

3 Simulation Results

A simulated phantom with a diameter of 80 mm ($2R'$) with background $\mu_a^0 = .005\ \mathrm{mm}^{-1}$, $\mu_s'^0 = 0.83\ \mathrm{mm}^{-1}$ [similar to the phantom in Fig. 2(a)] is used for generating[20] the simulated homogeneous flux density $\Phi^{\mathrm{homo}}_{\mathrm{sim}}$. We discretized the simulated phantom domain into 4032 elements and 2089 nodes and the finite element method (FEM) solution of light diffusion is obtained all over the domain.[2] Seven detector measurements at boundary nodes are taken (flux density) for each of the source locations [as shown in Fig. 1(b)]. An inhomogeneity (an object)

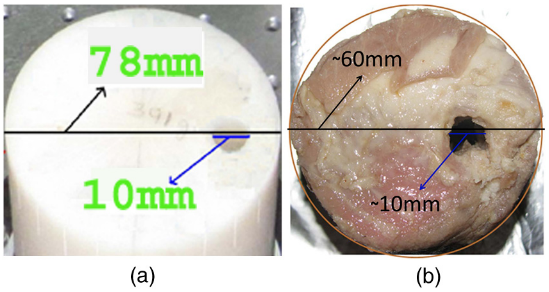

Fig. 2 (a) The tissue-mimicking phantom; (b) the pork tissue phantom.

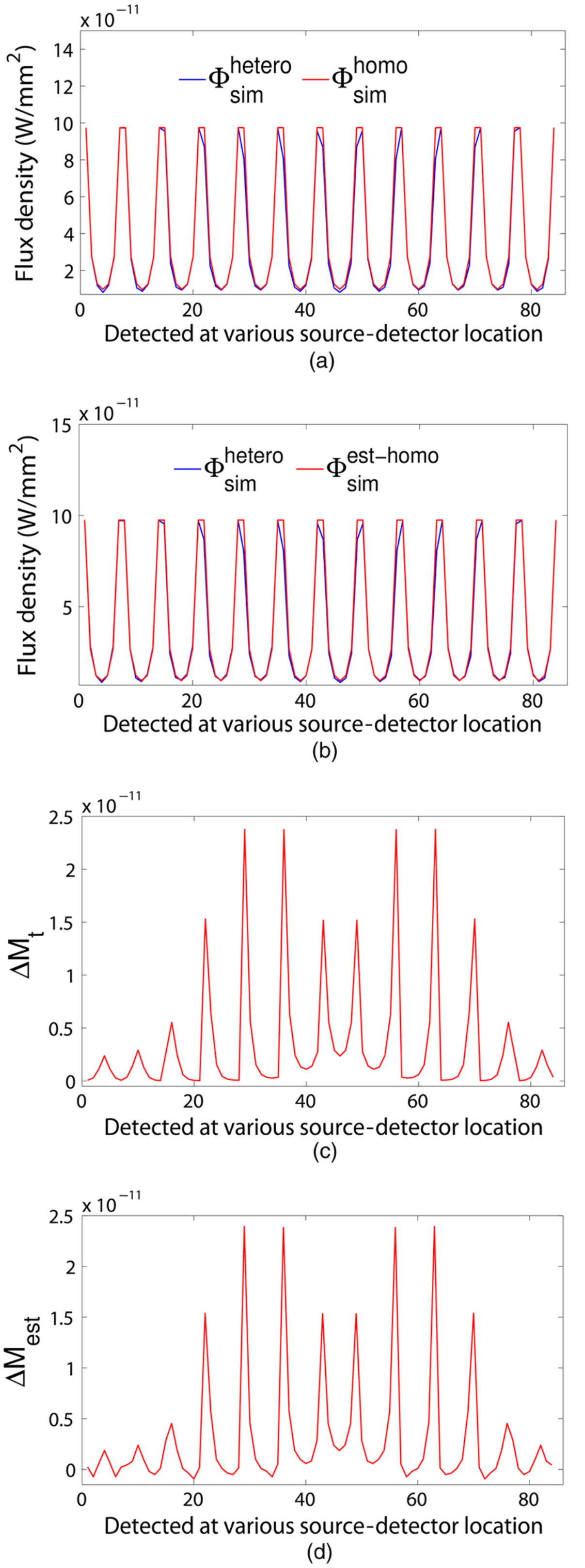

Fig. 3 (a) Simulated heterogeneous (blue line) and homogeneous (red line) flux densities, (b) simulated heterogeneous (blue line) and estimated homogeneous (red line) flux densities from the heterogeneous flux density [Eq. (8)], (c) the perturbation in data due to inclusion when the perturbation is measured with respect to the true homogeneous flux density, (d) the perturbation in data due to inclusion when the perturbation is measured with respect to the estimated homogeneous flux density.

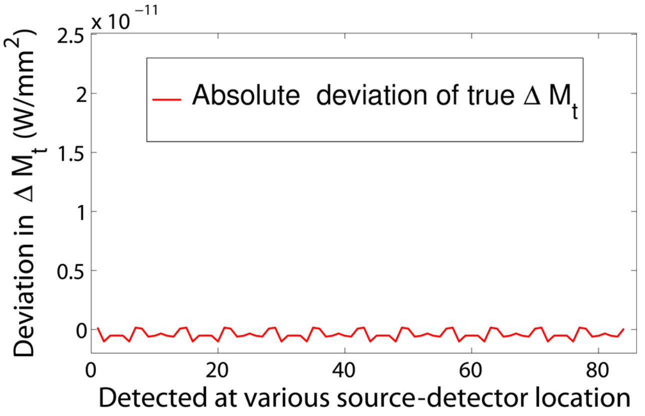

Fig. 4 The deviation of absolute mismatch (ΔM) when the perturbation/mismatch is obtained using estimated homogeneous flux density.

with a diameter of 8.2 mm (full width at half maximum) having $\mu_a^{\text{incl}} = .015\ \text{mm}^{-1}$ and the same value of μ_s' as background is introduced at (19.2,0) to generate a simulated heterogeneous flux density ($\Phi_{\text{sim}}^{\text{hetero}}$) [Fig. 3(a)].

The homogeneous flux density is estimated ($\Phi_{\text{sim}}^{\text{est-homo}}$) [Fig. 3(b)] from simulated heterogeneous flux density ($\Phi_{\text{sim}}^{\text{hetero}}$) by the proposed method [Eq. (7)]. The perturbation or mismatch (ΔM) of the flux density with inclusion is shown in Fig. 3(c) and 3(d), when the perturbation/mismatch of fluence is measured with respect to true homogeneous flux density ($\Delta M_t = \Phi_{\text{sim}}^{\text{hetero}} - \Phi_{\text{sim}}^{\text{homo}}$) and with estimated homogeneous flux density $\Delta M_{\text{est}} = \Phi_{\text{sim}}^{\text{hetero}} - \Phi_{\text{sim}}^{\text{est-homo}}$, respectively. The deviation of absolute mismatch (ΔM) is shown in Fig. 4, when we use the estimated homogeneous data. The mean error between the simulated homogeneous data and estimated homogeneous data $\bar{e} = \sum_{i=1}^{84} |(\Phi_{\text{sim}}^{\text{hetero}} - \Phi_{\text{sim}}^{\text{est-homo}})/\Phi_{\text{sim}}^{\text{homo}}|/84$ is found to be $\bar{e} \simeq 0.004$, which validates the homogeneous data estimation algorithm [Eq. (7)]. We have also placed multiple inhomogeneities (2) at (19.2,0) and (0,19.2), (3) at (19.2,0), (−19.2, 0) and (0, 19.2) and estimated $\Phi_{\text{sim}}^{\text{est-homo}}$ from $\Phi_{\text{sim}}^{\text{hetero}}$. The error is found to be low. The observations are tabulated for both trial and error, and effective perturbation (EP) strategies in Tables 1 and 2, respectively. The recovered absorption coefficients are obtained as 62%, 58%, and 61% of the original contrast, respectively. We have observed noisy images as the number of inclusions increases.

4 Experimental System and Phantom Preparation

A frequency domain noncontact DOT imaging system is designed and fabricated (Figs. 5 and 6) for conducting the experiment. A single-laser light source is used to irradiate the phantom, and a single detector moves around the phantom for collecting the exiting photon from the tissue boundary.[20,21,22] The light source is an intensity-modulated laser diode (HL7851G, Thorlabs, Newton, New Jersey), at a wavelength of 830 nm, of average power 4.3 mW, whose modulation frequency is 100 MHz. The diode is driven by a 50-mA DC current mixed with a 20 mA radio-frequency (rf) current on a Thorlabs TCLDM9 laser mount. The rf signal is from an ultrastable function generator (Tektronix AFG 3102, Tektronix, Beaverton, Oregon). In order to have a stable wavelength output, the laser diode is cooled by a Thorlabs TCM1000T cooler. The output from the laser diode is split using a 10:1 beam-splitter. The less-intense beam is fed to an avalanche photo-diode (APD) to generate a 100-MHz reference signal, and it is used as an input to the mixer (Fig. 5). The second input to the mixer is a 100.001-MHz rf signal from same function generator. The 1-KHz beat signal from the mixer output is used as a reference signal for the lock-in amplifier. The intense part of the light from the beam-splitter is coupled to a 3-mm diameter multimode fiber to illuminate the phantom and the exiting light at the phantom boundary is collected by a fiber bundle with a 5-mm diameter, which subsequently transmits the light to a detector, an IR-sensitive PMT from Hamamatsu (Shizuoka, Japan), which is gain-modulated at 100.001 MHz for our application. The dynode of the PMT is driven by a 100.001-MHz sinusoidal signal (second channel of Tektronix AFG 3102). The heterdyne signal of 1 KHz from the detector is fed to a lock-in amplifier, which also receives the reference signal from the APD. This facilitates the measurement of the exiting photon signal from the PMT. We have collected a set of 84 amplitude measurements (12 equally spaced source positions spanning the phantom surface multiplied by 7 detector measurements per source location).

The phantom is an artificial tissue-mimicking object whose background optical properties are similar to those of a tissue. They are fabricated[23] to mimic the absorption and scattering properties of the tissue. The cylindrical phantom is made of Araldite and a hardener whose scattering and absorption properties are tailored by mixing titanium dioxide powder and India ink, respectively. Here, 400 g of resign (C-51 Araldite resign, Atul Polymer, India) and India ink (0.25 ml 2%) are mixed thoroughly together with 1.3 g titanium dioxide until all the gas is released. Initially, 20 g of hardener (50% of total volume) is added to the mixture and mixed well, especially at the bottom. After proper mixing, the rest of the hardener is added to the main content and mixed thoroughly for 1 h until it gets hot and starts cooling down. Once the phantom is hardened enough, it is machined to cylindrical shape.

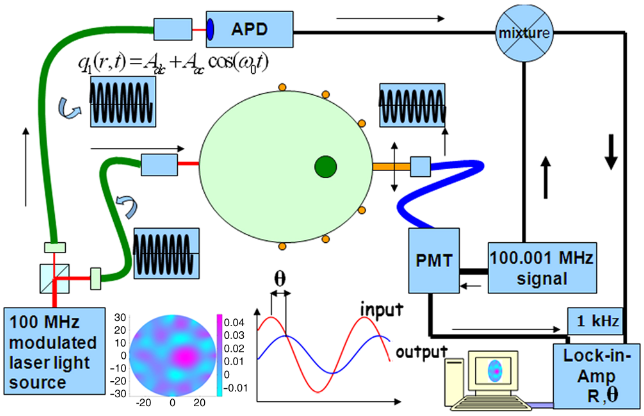

Fig. 5 Schematic model for a frequency domain DOT imaging system.

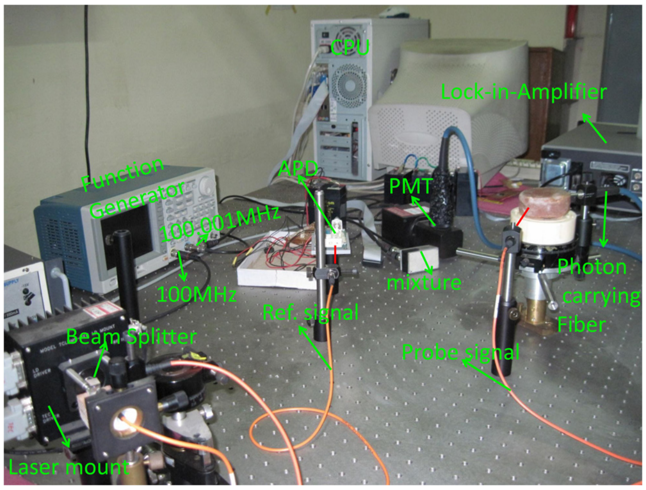

Fig. 6 The frequency domain experimental setup for DOT data measurements.

5 Experimental Results and Discussion

An NIR laser light modulated by a 100-MHz sinusoidal signal is used to estimate the background optical parameter by measuring the diffuse reflected photon at several locations away from the source.[18,20] The measured background absorption and scattering coefficient of an experimental tissue-mimicking phantom are found to be $\mu_a = 0.005\ \mathrm{mm}^{-1}$ and $\mu_s' = 0.83\ \mathrm{mm}^{-1}$ for the phantom shown in Fig. 2(a). Absorption and scattering

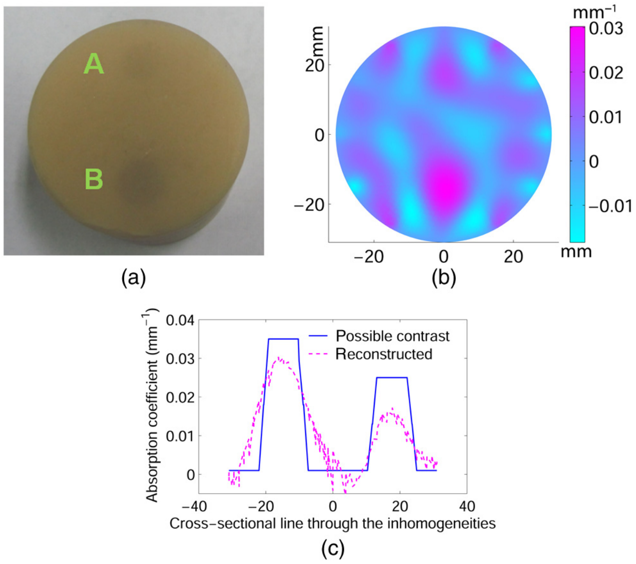

Fig. 7 (a) Two embedded inhomogeneities of 12 mm and 10 mm in diameter in a phantom of 60.6 mm diameter, 70.5 mm height. (b) Reconstructed image from calibrated data using measured heterogeneous data (using method 2). (c) The contrast variation along the cross-sectional line through the inhomogeneities (blue line) in the phantom. The line plot (purple dotted line) through the center of inhomogeneities of the reconstructed image shown in (b).

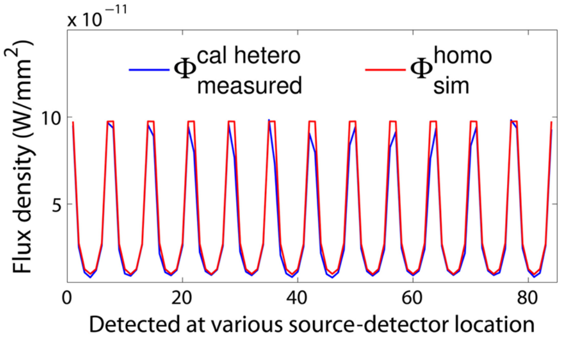

Fig. 8 Experimental calibrated heterogeneous flux density (blue line) when calibration is performed using experimentally detected homogeneous data [see Eqs. (3)–(6)]. The simulated homogeneous flux density is also shown (red line).

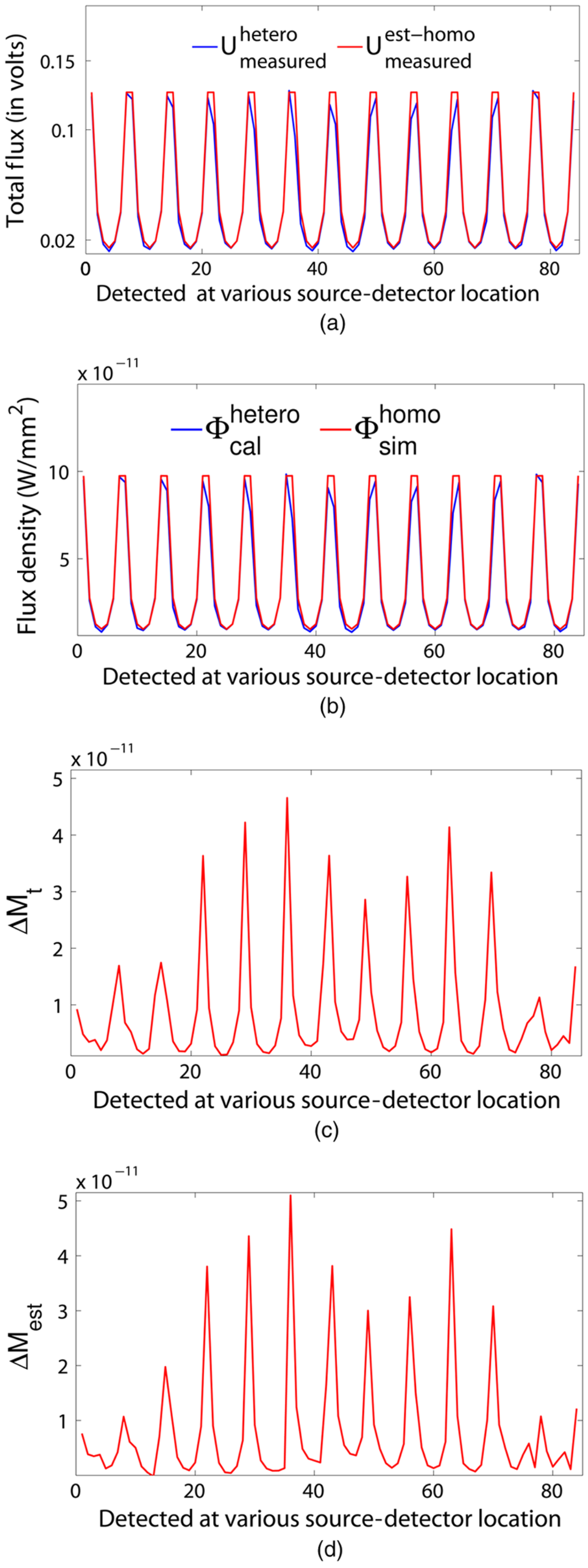

Fig. 9 (a) Experimentally detected heterogeneous data $({}^{k,d}U^{\text{homo}}_{\text{measured}})$ (blue line) and estimated experimental homogeneous data $({}^{k,d}U^{\text{est-homo}}_{\text{measured}})$ (red line) using Eq. (7). (b) Experimental calibrated heterogeneous flux density (blue line) using Eqs. (7) and (8) and simulated homogeneous flux density (red line). (c) Calibration is carried out using experimental homogeneous measurement. (d) Calibration is carried out using an estimated experimental homogeneous measurement.

coefficients of the phantom shown in Fig. 7(a) is found to be $\mu_a = 0.002\ \text{mm}^{-1}$ and $\mu_s' = 1.21\ \text{mm}^{-1}$, respectively. A small cylinder is drilled in the homogeneous phantom and is filled with 10% intralipid solution and India ink[24] to provide the inhomogeneous regions.

The frequency domain experimental setup is shown in Fig. 6. Experiments have been carried out for both regularly and irregularly shaped phantoms [Fig. 2(a) and 2(b)]. A cylindrical tissue-mimicking phantom (78 mm diameter, $\mu_a = 0.005\ \text{mm}^{-1}$, $\mu_s' = 0.83\ \text{mm}^{-1}$) [Fig. 2(b)] and an irregular cylindrical (dia ≈ 60 mm) pork flesh [Fig. 2(b)] (as a biological phantom) have been used. For the pork tissue phantom, because of the irregularity, the distance (r_d) from the detector to the sample surface varies from 1 mm ≤ to ≤5 mm. A 10-mm diameter inhomogeneity ($\mu_a^{\text{incl}} \simeq 0.03\ \text{mm}^{-1}$, made of ink, water, and intralipid)[24] is introduced to a tissue-mimicking phantom [Fig. 2(a)] and approximately 10 mm of fat is introduced inside the pork tissue (see Ref. 25 and Table 2) ($\mu_a = 0.006\ \text{mm}^{-1}$, $\mu_s' = 0.67\ \text{mm}^{-1}$).

We experimentally measured the exiting light amplitude for homogeneous ($U^{\text{homo}}_{\text{measured}}$) and heterogeneous ($U^{\text{hetero}}_{\text{measured}}$) phantoms by moving the detector over a constant radius. The theoretical flux density for homogeneous phantom and the experimental calibrated flux density [Eq. (5)] using detected experimental homogeneous data for regular phantom are shown in Fig. 8. Using Eq. (7), we estimated experimental homogeneous data ($U^{\text{est-homo}}_{\text{measured}}$) from detected heterogeneous data ($U^{\text{hetero}}_{\text{measured}}$), and our findings are shown in Fig. 9(a). The calibrated flux densities [for phantom Fig. 2(a)], obtained by Eqs. (4) and (7), are shown in Fig. 9(b). The perturbation of the flux density due to inclusion is shown in Fig. 9(c), when the perturbation (ΔM_t) is measured with respect to simulated homogeneous flux density and the calibration is carried out using an experimental homogeneous measurement. The perturbation of the flux density due to inclusion is shown in Fig. 9(d), when the perturbation (ΔM_{est}) is measured with respect to simulated homogeneous flux density, and the calibration is carried out using estimated homogeneous measurement with Eq. (7). The deviation of absolute mismatch (ΔM) is shown in Fig. 10, when we use the estimated homogeneous measurement.

The reconstructed image of a regular tissue-mimicking phantom when calibration is carried out with detected experimental homogeneous total flux and estimated total flux is shown in Fig. 11(a) and 11(b), respectively. The cross-section line plot

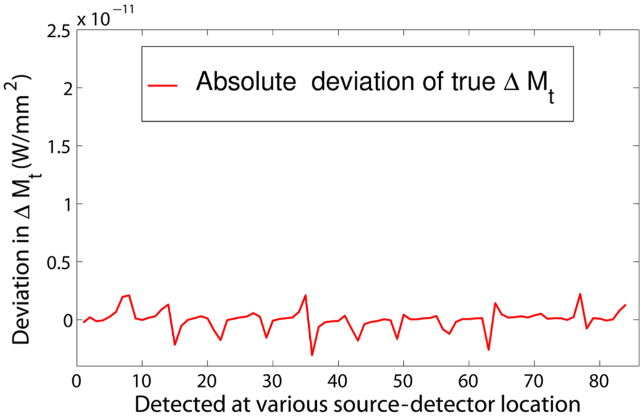

Fig. 10 The deviation of absolute mismatch when the perturbation/mismatch is obtained using an estimated homogeneous measurement.

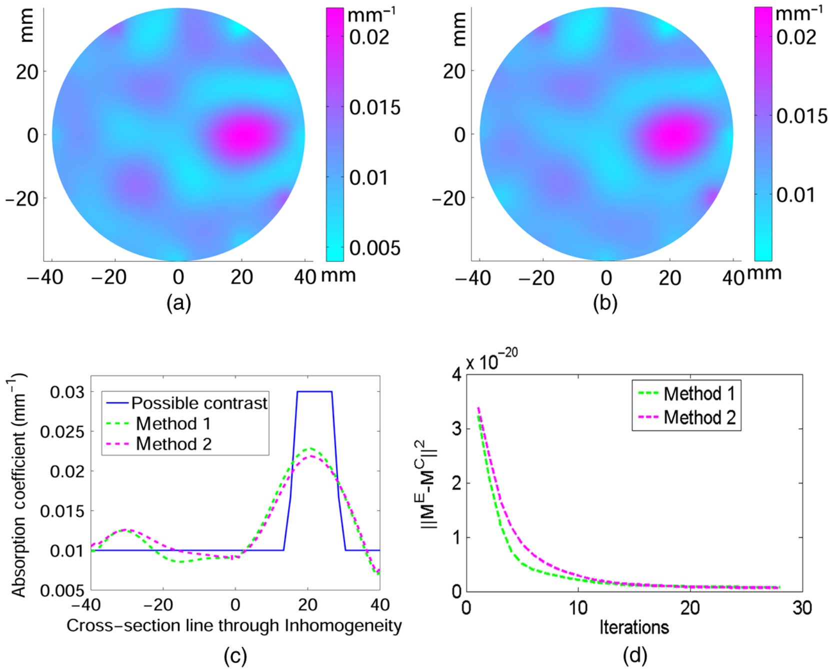

Fig. 11 Reconstruction image of a tissue-mimicking phantom with an embedded inhomogeneity [Fig. 2(a)] when the calibration is performed (a) with experimentally detected homogeneous data (using method 1), (b) with estimated homogeneous data (using method 2) (c) The contrast through the cross-sectional line through the center of inhomogeneity. (d) The variation in MSE with iterations.

through the inhomogeneity for both cases is shown in Fig. 11(c). The mean square error (MSE) with iteration is presented for both methods in Fig. 11(d). The results match very closely. The reconstructed image of the pork phantom, when calibration is carried out with experimental homogeneous total flux and estimated homogeneous flux, are shown in Fig. 12(a) and 12(b), respectively. The cross-section line plot through the inhomogeneity for both cases is shown in Fig. 12(c). Figure 12(d) shows the variation of the MSE with iteration. The reconstructed results with the estimated homogeneous data is bit noisy. This noise may be introduced during estimation due to more inhomogeneity in the background, as already analyzed and tabulated. For an irregular phantom, the small variation of geometrical shape matrix (r_d) may cause more inaccuracy in the homogeneous parameter estimation due to inappropriate free space photon propagation compensation.

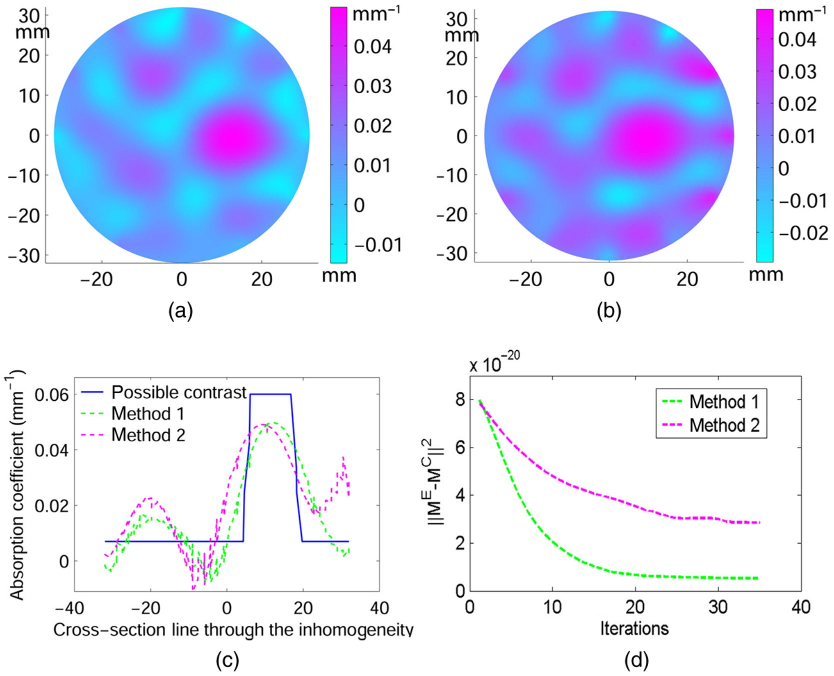

Fig. 12 (a) Reconstruction image of fat inserted inside the pork phantom when the calibration is performed with (a) experimentally detected homogeneous data (using method 1) and (b) estimated homogeneous data (method 2). (c) Cross-sectional line through the inhomogeneity. (d) The variation of MSE with iterations.

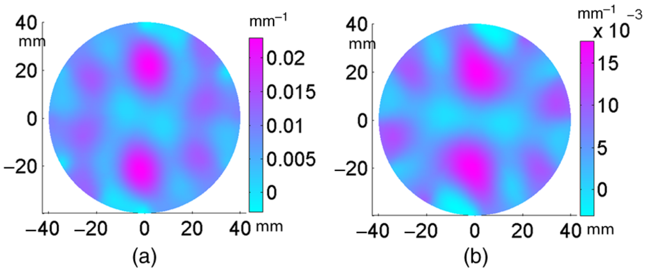

Fig. 13 A phantom with two embedded inhomogeneities. The reconstructed results when the calibration is performed with (a) experimentally detected homogeneous data (using method 1) and (b) estimated homogeneous data (using method 2).

Experiments are carried out with two embedded inhomogeneities made of India ink and 10% intralipid. The reconstructed results using measured homogeneous and estimated homogeneous data are shown in Fig. 13(a) and Fig. 13(b), respectively.

Apart from that, we used another 60-mm-diameter phantom [Fig. 7(a)] (background $\mu_a = 0.002\ \text{mm}^{-1}$, $\mu_s' = 1.21\ \text{mm}^{-1}$), where there were two embedded inhomogeneities of different absorption coefficients. The experimental homogeneous data for this phantom is not available because the inhomogeneities were already inserted during phantom fabrication. We used the proposed method to estimate the homogeneous flux density for calibrating the heterogeneous measurements. The phantom image and reconstructed images are shown in Fig. 7(a) and 7(b). The cross-sectional line plot through the inhomogeneities is shown in Fig. 7(c). The results show that the homogeneous data estimation and image reconstruction is possible even without measured homogeneous data. This result validates the estimation algorithms.

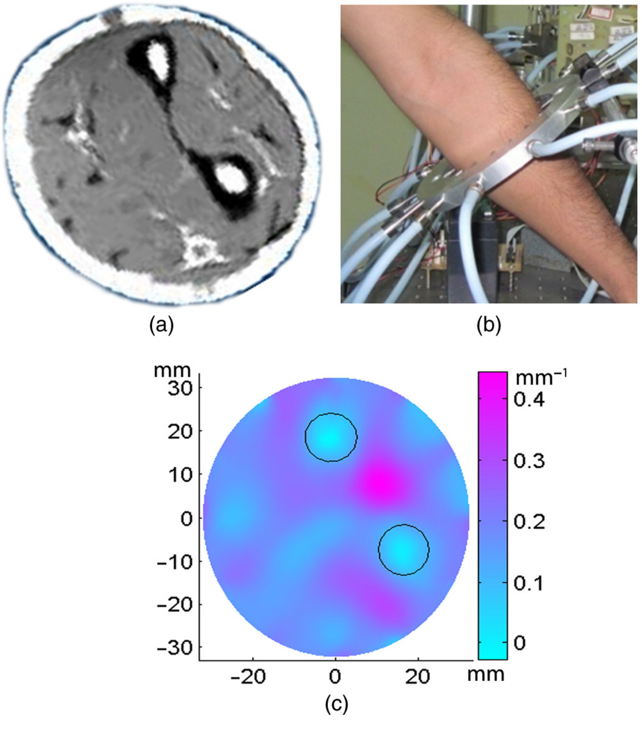

Fig. 14 (a) Cross-sectional MR image of a hand shows the bone locations. (b) Photograph of the hand-scanning DOT imaging system. (c) Reconstructed diffusion coefficient ($\kappa(r)$), when flux density is estimated using method (2). The diffusion through the bones is almost zero and shows the location of the bones.

The diffusion coefficient $\{\kappa(r) = 1/3[\mu_a(r) + \mu_s'(r)]\}$ distribution of the human hand has been reconstructed to demonstrate the ability of the proposed algorithm. The experimental homogeneous data from the hand phantom [Fig. 14(b)] is not available. Even when the measured homogeneous data is not available, we used the proposed "method 2" to estimate the homogeneous flux density for calibrating the heterogeneous measurements. The MR image and DOT reconstructed images are shown in Fig. 14(a) and 14(c), respectively. The locations of the bone in the hand are presented through the $\kappa(r)$ distribution. It shows that light cannot diffuse through the bone. The reconstructed image shows that there is more diffusion of light between the bones, where there are less dense tissue and more hollow spaces. The results with the pork tissue phantom and human hand image show that the homogeneous data estimation and absolute image reconstruction is possible in clinic, even when measured homogeneous data is available.

6 Conclusions

We have shown theoretically [Eqs. (3)–(8)] and experimentally that the proposed simple models estimate the absolute flux density (Φ) from detected total flux (U_{measured}). The estimated flux density with the proposed methods matches very closely with the simulated flux density. The reconstructed results for both the regular tissue-mimicking phantom and pork phantom are well resolved and localized when heterogeneous data is calibrated with experimentally measured homogeneous data. When the experimental homogeneous data are not available, the proposed statistical averaging method estimates the experimental homogeneous data from measured heterogeneous data and the MSE is found to be less than 0.005. The lower the effective perturbation is, the better the estimation is. The estimated homogeneous data match very closely to both theoretical and the experimental homogeneous data for a regular-shaped phantom [Fig. 2(a)]. Reconstructed results of a regular cylindrical phantom show similar results [Fig. 2(a)], when calibrated with and without prior knowledge of the experimental detected homogeneous data. However, the reconstructed result of the pork phantom matches closely when it is calibrated with estimated homogeneous data. Because of irregular shape of pork phantom, the distance between phantom surface and detector varies from 1 to 5 mm. The estimation of homogeneous data from heterogeneous data is carried out by projecting the photon flux from an irregular shape to a regular constant circular radius. Φ varies nonlinearly with distance (r) and with optical parameters. The more irregular the phantom, the more discrepancy occurs in the calibrated flux density. The estimation of homogeneous data will be more accurate if the phantom is regular. The estimation of the homogeneous flux density in the proposed method will be more accurate if the irregularity of the phantom is less. With 1 to 5 mm r_d variation, we got reasonably good reconstruction results for the pork tissue phantom and the cross-section of the human hand image.

Acknowledgments

The authors acknowledge the support by the Department of Science and Technology, Government of India, via Grant No. DST 1163.

References

1. A. P. Gibson, J. C. Hebden, and S. Arridge, "Recent advantages in diffuse optical tomography," *Phys. Med. Biol.* **50**, R1–R43 (2005).
2. S. Arridge and J. C. Hebden, "Optical imaging in medicine: II. Modelling and reconstruction," *Phys. Med. Biol.* **42**(5), 841–853 (1997).
3. S. Arridge, "Optical tomography in medical imaging," *Inverse Probl.* **15**(2), R41–R93 (1999).
4. J. Ripoll, R. Schulz, and V. Ntziachristos, "Free-space propagation of diffuse light: theory and experiments," *PRL* **91**(10), 103901 (2003).
5. B. J. Tromberg et al., "Non-invasive measurements of breast tissue optical properties using frequency-domain photon migration," *Phil. Trans. Royal Soc. London B* **352**(1354), 661–668 (1997).
6. A. H. Hielscher et al., "Near-infrared diffuse optical tomography," *Dis. Markers* **18**(5–6), 313–337 (2002).
7. M. Schweiger et al., "Image reconstruction in optical tomography in the presence of coupling errors," *Appl. Opt.* **46**(14), 2743–2756 (2007).
8. E. M. C. Hillman et al., "Calibration techniques and datatype extraction for time-resolved optical tomography," *Rev. Sci. Instrum.* **71**(9), 3415–3427 (2000).
9. T. Tarvainen et al., "Computational calibration method for optical tomography," *Appl. Opt.* **44**(10), 1879–1888 (2005).
10. C. Li and H. Jiang, "A calibration method in diffuse optical tomography," *J. Opt. Soc. Am. A* **6**(9), 844–852 (2004).
11. S. Jiang et al., "Quantitative analysis of near-infrared tomography: sensitivity to the tissue-simulating precalibration phantom," *J. Biomed. Opt.* **8**(2), 308–315 (2003).
12. C. Vinegoni et al., "Normalized born ratio for fluorescence optical projection tomography," *Opt. Lett.* **34**(3), 319–321 (2009).
13. T. O. McBride, "Spectroscopic reconstructed near infrared tomographic imaging for breast cancer diagnosis," Ph.D. Thesis, Dartmouth College, pp. 90–103 (2001).
14. D. A. Boas and T. Gaudette, "Simultaneous imaging and optode calibration with diffuse optical tomography," *Opt. Express* **8**(5), 263–270 (2001).
15. A. Joshi et al., "Fully adaptive FEM-based fluorescence optical tomography from time-dependent measurements with area illumination and detection," *Med. Phys.* **33**(5), 1299–1310 (2006).
16. N. Gao, S. A. Zhu, and B. He, "Estimation of electrical conductivity distribution within the human head from magnetic flux density measurement," *Phys. Med. Biol.* **50**(11), 2675–2687 (2005).
17. J. Laufer et al., "Quantitative determination of chromophore concentrations from 2D photoacoustic images using a nonlinear model-based inversion scheme," *Appl. Opt.* **49**(8), 1219–1233 (2010).
18. S. Fantini et al., "Quantitative determination of the absorption spectra of chromophores in strongly scattering media: a light-emitting-diode based technique," *Appl. Opt.* **33**(22), 5204–5213 (1994).
19. B. Kanmani and R. M. Vasu, "Diffuse optical tomography using intensity measurements and the a priori acquired regions of interest: theory and simulations," *Phys. Med. Biol.* **50**(2), 247–264 (2005).
20. S. K. Biswas, K. Rajan, and R. M. Vasu, "Diffuse optical tomographic imager using a single light source," *J. Appl. Phys.* **105**(2), 024702 (2009).
21. S. K. Biswas, K. Rajan, and R. M. Vasu, "Practical fully 3-D reconstruction algorithm for diffuse optical tomography," *J. Opt. Soc. Am. A* **29**(6), 1017–1026 (2012).
22. S. K. Biswas et al., "Accelerated gradient-based diffuse optical tomographic image reconstruction," *Med. Phys.* **38**(1), 539–547 (2011).
23. B. W. Pogue and M. S. Patterson, "Review of tissue simulating phantoms for optical spectroscopy, imaging and dosimetry," *J. Biomed. Opt.* **11**(4), 041102 (2006).
24. M. Autiero et al., "Determination of the concentration scaling law of the scattering coefficient of water solutions of intralipid at 832 nm by comparision between collimated Detection and Monte Carlo simulations," *Lasers Surg. Med.* **36**(5), 414–422 (2005).
25. M. R. Armfield et al., "Analysis of tissue optical coefficients using an approximate equation valid for comparable absorption and scattering," *Phys. Med. Biol.* **37**(6), 1219–1230 (1992).